# A study of the mechanical properties of Al6061-Zr_1, 2 alloy processed by laser beam melting

Mathieu Opprecht, Guilhem Roux, Jean-Paul Garandet, Camille Flament

# A study of the mechanical properties of Al6061-$Zr_{1,2}$ alloy processed by laser beam melting

Mathieu Opprecht, Guilhem Roux, Jean-Paul Garandet, Camille Flament

Mathieu OPPRECHT, Université Grenoble Alpes, CEA LITEN, Grenoble, France, mathieu.opprecht@gmail.com
Guilhem ROUX, Université Grenoble Alpes, CEA LITEN, Grenoble, France, guilhem.roux@cea.fr
Jean-Paul GARANDET, Université Grenoble Alpes, CEA LITEN, Grenoble, France, jean-paul.garandet@cea.fr
Camille FLAMENT, Université Grenoble Alpes, CEA LITEN, Grenoble, France, camille.flament@cea.fr

Corresponding author: mathieu.opprecht@gmail.com/ 04.38.78.47.69

DOI: https://doi.org/10.1007/s11665-022-07218-0

## Highlights

- Comprehensive characterization of an additively manufactured modified A6061 alloy.
- Correlation between microstructural features and mechanical properties.
- 3D-printed mechanical response up to $\sigma_Y$=340MPa and $\sigma_{UTS}$=350MPa.
- Comparison of the atomisation vs mixing techniques to design new alloys for powder layers based processes.

## Abstract

The present paper proposes an experimental study to determine the mechanical properties of an additively manufactured modified A6061 alloy, where the addition of 2 volumic % of Yttrium Stabilized Zirconium (YSZ) to Al6061 base powder allows to fully remove cracks during Laser Beam Melting processing. To this end, Vickers tests, tensile tests, Charpy tests and microstructural analyses are used. With respect to the building direction, a quasi-isotropic response is highlighted, with properties (engineering yield and ultimate strengths) higher than the wrought 6061 alloy. This improvement can be attributed to the extra-fine microstructure, a large dislocation density, and a specific precipitation/solution trapping behaviour associated with the Zr addition. Besides, the alloy showed excellent tensile response reproducibility. Thereafter, effect of post-heat treatments are investigated. Classic T6 from wrought alloys practice allowed to precipitate well known and reported nano β''-$Mg_xSi_y$ phases, improving the yield and ultimate strengths, but at the expense of significant grain coarsening. The mechanical properties are further increased through an adapted heat-treatment, specifically designed for this Al6061 modified alloy. $Al_3Zr$ hardening nanoprecitates are responsible of the improved yield response observed after an annealing for 2 hours at 400°C. The competition between these different hardening precipitation phases (nano β''/ nano $Al_3Zr$) is finally discussed.

## Keywords

Laser Beam Melting / Aluminium Alloy / Strength response / Hot cracking / Rapid Solidification /Powder mixing / Post heat-treatments.

## 1. Introduction

For over sixty years, aluminium ranks at second only to iron in the metal market [1], mainly thanks to its low specific density combined with good electrical and thermal conductivities. This is particularly true for the 6061 precipitation-hardened aluminium alloy, widely used in construction, automotive and aerospace industries [2]. The major alloying elements Mg and Si lead to precipitation strengthening during an ageing heat treatment, mostly through widely studied needle-shaped β'' nano-precipitation [3]. These precipitates and their strengthening contribution are particularly sensitive to the ageing temperature [1]. According to the precipitation sequence, metastable β'' phases rapidly evolve in rod-shaped β' and further on in $Mg_2Si$ precipitates [4–7]. Both of them are less efficient than β'' in terms of hardening.

More recently, Laser Beam Melting (LBM) and on a larger scale 3D printing of aluminium alloys have attracted increasing attention in the scientific and industrial communities [8,9]. As a matter of fact, 3D printed alloys display many specific features, with novel microstructure induced by rapid solidification, which improves mechanical response [10–12]. However, the severe thermal conditions induced by the LBM process introduce new challenges. Structural aluminium grades are suffering from the hot cracking phenomenon. Cracks are propagating along columnar grains oriented in the building direction [13–15], and are attributed to solidification cracking [16]. 6061 alloy is particularly susceptible to this phenomenon ([17],[18]), especially during LBM processing.

In this respect, based on the knowledge from welding configurations, most of the implemented strategies are focusing on grain refinement to reduce this hot cracking sensitivity. A possible solution to address the problem relies on the reduction of the thermal gradient. Uddin et al. [19] recently succeeded in producing 6061 crack free components through the use of a 500°C heating plate. However, it can be argued that this heating plate strategy has its own limits, especially for the fabrication of elongated parts, and raises a number of issues regarding process control. Another potential strategy is to increase the nucleant sites density in front of the liquid/solid interface. A number of research papers show interesting results with zirconium or scandium additions, either by direct inclusion during the powder atomisation step, or by indirect addition (powder mixing or coating) further in the process [14,20–27], [28],[29],[30],[31]. More specifically, a duplex microstructure is often observed, with a band of equiaxed grains decorating the bottom of each melt pool, and with columnar growth resuming towards the free surface. The accepted reason is a variation of $\alpha_{Al}$ nucleant sites (squared $Al_3Zr$ particles) density for growth with melt pool depth. With the use of standard nucleation theory, Opprecht et al. have recently demonstrated that such variation is due to the increase of the cooling rate towards the free surface [32].

In a recent interesting paper, Mehta et al. investigated the LBM processing of a gas atomised Zr-modified Al6061 powder [33]. The addition of 1wt% of Zr lead to the suppression of the hot cracking phenomenon. Yield strength, tensile strength and ductility of respectively 210 MPa, 268 MPa, and 26.5% were reported, better that the wrought Al6061 ones. A T6 heat treatment enabled to further improve the yield response up to 300MPa.

Another original method to avoid this hot cracking issue for structural grades in LBM has been developed by Opprecht et al. [15], focused on the 6061 alloy. The proposed solution is to introduce Yttrium Stabilized Zirconia (YSZ) to Al6061 base powder using a dry mixing (Turbula®) procedure. The addition of 2 vol% allows to fully remove cracks. At 1vol%, a discontinuous band of equiaxed grains appears at the bottom of some melt pools. From 2vol% and above, this strip

becomes continuous at each melt pool boundary and prevents the formation of cracks associated to the existence of an elongated columnar structure. TEM investigations show that Zr combines with Al to form the $\alpha_{Al}$ nucleant phase $Al_3Zr$ [34].

Following this study, the emphasis of the current work is on the mechanical response of this 3D printed modified Al6061 material. The first purpose is to compare the mechanical response of wrought Al6061 alloy with a 3D printed modified Al6061 one. A second and more ambitious objective is to understand and take advantage of the Zr addition through an adapted heat treatment designed for this alloy, the idea being to see if this additively manufactured material can be optimized in terms of mechanical properties.

More specifically, the impact of building direction and the use of recycled powder on mechanical properties (Vickers and tensile tests) will be investigated on as-built material. Toughness analysis (Charpy tests) of this as-built state will also be presented. Afterwards, the effect of thermal heat treatments on mechanical properties will be correlated to microstructure characterizations. Finally, the main contributions for the yield strength of this modified 3D printed Al6061 alloy will be investigated. More specifically, the competition between the growth kinetics of the various hardening phases will be discussed. Finally, the approach will be discussed in view of the results recently obtained by Mehta et al. [33] on a similar Zr-modified Al6061 alloy to check the potential of the mixing powder preparation route as compared to the atomization technique used in [33], a key point in the view of further alloys developments. Indeed, the Zr incorporation route may impact the final 3D printed product. Nowadays, such comparison cannot be found in the literature, which clearly represents an innovative aspect of the present work

## 2. Material and method

### 2.1 Material

A gas atomized Al6061 powder (TLS Technik Bitterfeld©) was mixed with 2 volumic % of Yttria-Stabilized Zirconia (YSZ) powder (INNOVNANO©). It is important to note that the Zr content of the Al6061+2vol% YSZ LBM printed alloy is equal to 1.2wt% (ICP measurement, see [15]). Thereafter, Al6061-$Zr_{1.2}$ alloy refers to the Al6061+2vol% YSZ alloy. The Al6061 powder is globally spherical and has a $D_{10}$, $D_{50}$ and $D_{90}$ respectively equal to 26 µm, 41 µm and 61 µm (dry Malvern laser scattering measurement). Its chemical composition (wt%) is summarized in Table 1. The YSZ powder (94.3wt% of $ZrO_2$ + 3.6wt% of $Y_2O_3$) has a unit size of about 60 nm. The mixing step was performed in a Turbula® setup. The homogeneity of the mixing was characterized through SEM images, optical granulometries and ICP measurements in a previous work [15].

Figure 1 presents SEM images of the Al6061-$Zr_{1.2}$ powder, after the mixing (left) and after one recycling cycle.

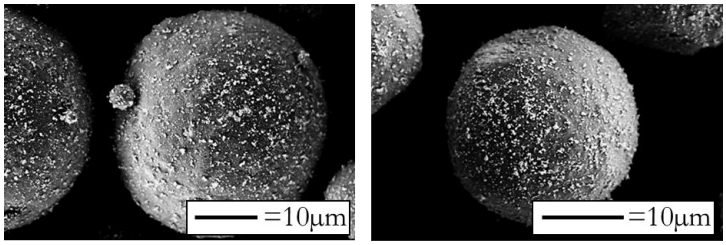


*Figure 1 : Scanning Electron Microscopy acquisition showing morphology of Al6061-$Zr_{1.2}$ mixed powders, left after the mixing and right after recycling.*

The overall spherical morphology of the 6061 powder is not altered by the mixing step, just like the spreadability of the Al606-$Zr_{1.2}$ powder. Note that specific flowability tests were not carried out, the conclusion was based on visual observations. On this point, some authors have demonstrated that such a coating even increases powder spreadability ([35,36]), a key feature for powder layer based processes (including LBM). The second important result regards the good YSZ particles gripping, even after handling and sieving steps (Figure 1).

## 2.2 Method

Al6061-$Zr_{1.2}$ samples were additively manufactured using a SLM Solutions SLM125HL machine. The machine was operated with hatch spacing of 100µm, layer thickness of 20 µm, laser speed of 700 mm/s and laser power of 216 W. Note that theses parameters come from the optimisation study carried out in [15]. Using this optimized set, specimens with dimensions 10 x 10 x 10 $mm^3$ were produced for microstructural analysis. A reference cube was analysed through ICP-OES. The results shown in Table 1 highlight that relative concentrations with respect to the powder reference are not affected by the 3D printing process, except for the Mg element (-33%, wt%, [15]). Such a variation can likely be correlated to a differential evaporation of Mg, due to its low boiling point. The oxygen increase can be related both to the addition of YSZ particles, which may release O in the melt pool, and also to the atmosphere in the fabrication chamber.

| | Al | Si | Mg | Cr | Fe | Mn | Cu | Zr | Y | 0 |
|---|---|---|---|---|---|---|---|---|---|---|
| 6061 TLS powder | Bal | 1.02 | 0.78 | 0.18 | 0.144 | 0.03 | 0.427 | / | / | 0.05 |
| Al6061-$Zr_{1.2}$ cube | Bal | 1.09 | 0.55 | 0.172 | 0.141 | 0.03 | 0.421 | 1.19 | 0.05 | 0.13 |

*Table 1 : ICP-OES measurements of the TLS 6061 powder and a 3D printed Al6061-$Zr_{1.2}$ cube.*

For this optimized set, a maximum densification was found around 99% (Archimedes method). However, the determination of the theoretical volumic mass of this alloy from powder composition is questionable, since it is based on an also questionable volume additivity rule. Optical micrographs further confirmed a really good densification (*i.e.* > 99.8%) [15], with the presence of small spherical defects mainly attributed to occluded gases common in Al based materials [37].

For the above mentioned cubic samples, a scan strategy with unidirectional scanning vector (no rotation between consecutive layers) was used to facilitate the microstructural analysis. For the tensile and Charpy tests, specimens of dimensions 12 x 12 x 60 $mm^3$ and 10 x 10 x 55 $mm^3$ were built, with a different scanning strategy. A checkered pattern, with square islets of 5 mm randomly distributed from one layer to another was used to be more representative of industrial components lasing strategy. In each islet, bidirectional scanning vectors melt the powder, with a 200µm covering between islets (see Figure 2).

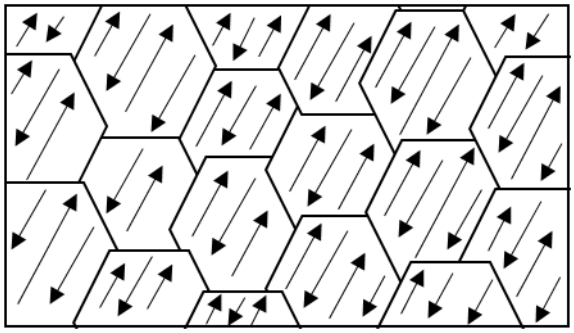

*Figure 2 : Scanning strategy used for tensile and Charpy specimens.*

Various post heat treatments (HTs) were implemented. A classic T6 HT has been applied to the 3D printed Al6061-$Zr_{1.2}$ alloy. It consists in a precipitate dissolution step (530°C for 5 hours), quench (into water), and ageing at 175°C for 9 hours. The Vertical Pyrox© furnace has been used, samples were placed in a quartz tube. As-built Al6061-$Zr_{1.2}$ samples have also been heat treated without the precipitate dissolution step at three ageing temperatures, *i.e.* 175°C, 300°C, 400°C for several durations in a tubular furnace.

Samples are cold mounted in epoxy resin mixed with a curing sealant. Then the surface were mirror polished using a Presi Mecatech Z34 machine. The procedure includes two SiC papers and two polishing pads (ADR2 3 µm and TFR 1µm) before a finishing step with 0.03 µm colloidal silica. Microstructures were observed using a LEO 1530 VP Gemini Field Effect Gun (FEG) and a MERLIN (ZEISS) scanning electron microscope (SEM), equipped with an Oxford detector. EBSD acquisitions were performed at 20 kV with step sizes of 0.3–0.4µm (x250) magnification, for a specimen tilted at 70° and a dwell time around 40ms. The post processing was performed on HKL software (Channel 5) with grain boundaries defined for misorientation higher than 15°. The indexing rate was above 85%.

The Focused Ion Beam (FIB) lift out approach was employed (Zeiss 550 FIB-SEM instrument) to prepare TEM lamellas in material area of interest. Scanning Transmission electron microscopy (S-TEM) investigations were conducted with a Thermo-Fisher Osiris Tecnai instrument, equipped with a X-FEG source and operating at 200 kV. STEM images were acquired on bright field (BF) and high angular annular dark field (HAADF) detectors. Energy dispersive X-ray spectroscopy (EDX) hyper-maps were recorded with Esprit 1.9 software (Brüker).

Micro-Vickers hardness were measured on a Matsuzawa MMT-X7B micro durometer, with a 200 g loading during 15 s. Pre-polished cubes (until SiC 4000 paper) in the YZ plane (Z being the building direction) were used for all measurements. With respect to the polished mirror norm, the reported hardness values can possibly be slightly overestimated. However, the procedure is expected to be adequate for comparative purposes. The following values correspond to a 10 measurements average, the reported errors bars being calculated from the standard deviation. Measurements points were selected, with the objective to cover the whole specimen sample. Room-temperature tensile tests were performed according to the EN ISO 6892-1 norm, on dumbbell specimens of circular cross section gauge diameter and length of respectively (5 mm and 28 mm). Charpy tests were conducted according to the EN ISO 148-1 norm, with a V notch machined on the samples prior to the experiments.

## 3. Results

This section starts with the investigation of the mechanical response of the as-built 3D printed Al6061-$Zr_{1.2}$ alloy. 3D printed specimens densification was found around 99% (optical micrographs method). The effect of anisotropy and the impact of recycled powder are presented through hardness, tensile response and microstructure analysis. Then, the influence of post HTs is examined, firstly based on classic T6 HT for wrought 6061 alloy. Secondly, a larger study of several HTs is undertaken, in order to identify an optimized HT, which is further characterized in detail.

### 3.1 As built

#### 3.1.1 Microstructure

The microstructure of the 3D printed as-built Al6061-$Zr_{1.2}$ alloy has been described in [15]. First of all, the 1.2 wt% Zr addition results in a duplex microstructure in each melt pool, with a band of small equiaxed grains at the bottom and the resumption of the columnar growth towards the center (see Figure 6 or [15]). The reasons for such microstructure have been detailed in [32]. In equiaxed regions, cubic shaped $Al_3Zr$ intragranular precipitates of circa 100 nm length are detected. On the contrary, the Zr is trapped into solid solution in columnar grains. Mg-Si large precipitates (>50nm) were detected in both regions, meaning that Mg and Si elements are not fully trapped in solution during the 3D printing process. Some dispersoids (Al, Fe, Si, Cr, Mn rich precipitates) are also detected (see for example Figure 3).

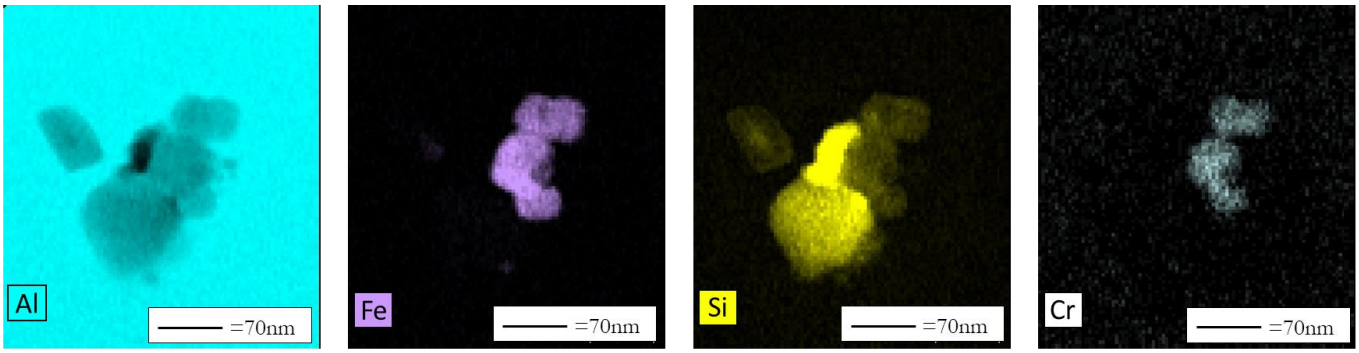


*Figure 3 : Dispersoid precipitate with STEM-EDX maps of Al, Fe, Si, and Cr elements.*

a) Grain size

The determination of a characteristic grain size is necessarily somewhat arbitrary due to the presence of both equiaxed and columnar grains in the microstructure. However, this feature is necessary to estimate the grain size contribution to the yield strength (4.1.2). Opprecht et. al [15] proposed an elliptic fitting method to collect both length and width informations for columnar grains. These results have been used in this work to determine an equivalent grain size according

to the tensile direction. When the specimen is horizontally 3D printed, the width of the columnar grains and the diameter of the equiaxed ones are considered. It leads to a mean grain size of 0.9 µm, considering a volumic equiaxed grains fraction equal to 50% [15]. When the specimen is vertically 3D printed, the length of the columnar grains and the diameter of the equiaxed ones are used, leading to a mean grain size of 3.3 µm. For these calculations, circa $10^4$ grains were analysed through an EBSD map taken at x750 magnification.

b) Dislocation density

Three dislocations types are often encountered in samples solidified from the melt. The first one corresponds to the bundles that constitute the grain boundaries. A related type can be found along solidification cells in a given grain [27]. It should be however noted that in the 3D printed Al6061-$Zr_{1.2}$ samples, solidification cells were never clearly observed. The third type is the intra-grain forest dislocations as observed in Figure 4. The KAM (Kernel Average Misorientation) technique is employed to evaluate an effective intra grain dislocation density (since it does not consider large angle grain boundaries) useful to estimate the yield strength contribution [38]. It should be stressed that this approach may underestimate the overall dislocation density as it does not take into account the forest contribution. To get a more accurate measurement, other techniques such as TEM/XRD would be needed, but the acquisition of statistically relevant data would require a considerable amount of data. As an emerging standard, KAM is likely helpful for comparative purposes.

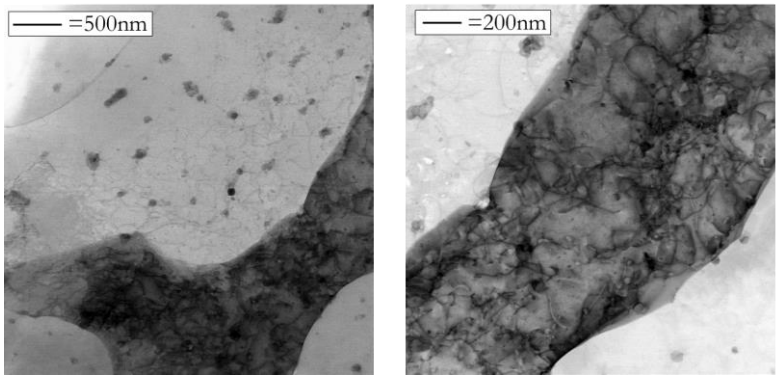


*Figure 4 : BF-TEM images of a columnar region of the as-built 3D printed Al6061-$Zr_{1.2}$ showing the intra-granular forest dislocations.*

Thanks to a post processing on Brüker© software, this method estimates the local misorientation of a pixel with regards to neighboring ones (Figure 5). The mean local misorientation (θ) can then be linked to the effective dislocation density ($\rho_0$) through the following relation [38]:

$$\rho_0 = \frac{2\sqrt{3}}{3} \times \frac{\theta}{bh} \qquad \text{Eq. 1}$$

*b* is the Burger vector of the $\alpha_{Al}$ structure (0.284nm) and *h* the EBSD acquisition pixel size. For the statistical evaluation of θ, an EBSD map recorded in the YZ plane is used (Figure 5). This method requires both high magnification (x750 here) and small pixel size (100nm here) to ensure a good order of magnitude measurement accuracy.

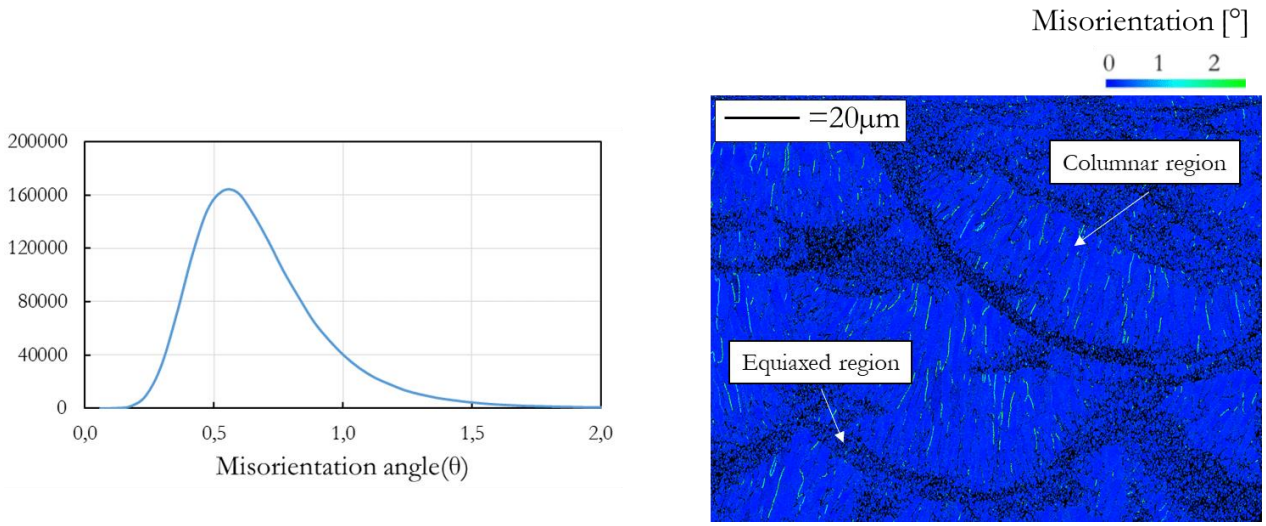


*Figure 5 : Local misorientation repartition deduced from an EBSD map of the as built 3D printed Al6061-$Zr_{1.2}$ (x750, pixel size: 100nm).*

The mean angle of misorientation is estimated to be 0.6° for the as built 3D printed Al6061-$Zr_{1.2}$, leading to a dislocation density roughly equal to $5x10^{14}m^{-2}$. Such a high density is very similar to that observed on other metallics alloys processed with LBM (see literature examples [39,40]). As previously mentioned in the literature [24], forest dislocations are not observed in the fine equiaxed grain regions (see Figure 5).

### 3.1.2 Vickers hardness

Micro-hardness measurements have been performed along a cube depth, in the YZ plane. The as-built additively manufactured Al6061-$Zr_{1.2}$ alloy has a much higher hardness (namely 90±2 HV) compared with wrought Al6061 alloy (≈30HV, ASM norm [41]). Measurements taken along the cube depth did not evidence any trend for hardness variation.

### 3.1.3 Tensile response

For illustrative purposes, the tensile properties are compared to the conventional Al6061 in annealed (O) – "soft" condition. The Al6061-$Zr_{1.2}$ alloy has higher strength than the wrought Al6061 alloy (bare product [41]). A strong increase of the engineering yield strength (from $\sigma_y$=55 MPa to $\sigma_y$=241 MPa) and engineering ultimate strength (from $\sigma_{UTS}$=124 MPa to $\sigma_{UTS}$=266 MPa) is noticed. This variation is, as expected, to the detriment of the ductility (from 25% to 17%). Note that the unconventional curve shape has already been observed for other high strength aluminium alloys processed by LBM [24] and can be attributed to Lüders band propagation, induced by the Portevin–Le Chatelier effect (successive serrations) [24], [42], [43]. Jia et al. [24] suggested that these bands formation might be associated with the release of dislocations from the solute atoms (or possibly some precipitates) that are binded around them. These effects lead to the presence of yielding peaks.

Interestingly, the standard deviation among the five tensile specimens tested remains very small for the engineering yield and ultimate strengths (±2MPa) and limited for the ductility (±2%).

Recycled powder (sieved at 75µm) has been used to horizontally print three new tensile specimens. Their mechanical response remains really close to that of the non-recycled powder reference, namely $\sigma_y$=244MPa, $\sigma_{UTS}$=268MPa and $\varepsilon$=18.5%. In addition, no significant variation has been observed between the three tensile specimens (±2MPa for $\Delta\sigma_y$ and $\Delta\sigma_{UTS}$, ±1% for $\Delta\varepsilon$).

Three specimens have also been printed vertically (*i.e.* along Z direction) with recycled powder. A small reduction of the engineering yield strength (namely from $\sigma_y$=241MPa to $\sigma_y$=224MPa) is observed. This can be possibly attributed either to defects alignment or columnar grains. Again, a good repeatability has been highlighted among the three samples (±1 MPa for $\Delta\sigma_y$ and $\Delta\sigma_{UTS}$, ±1% for $\Delta\varepsilon$). In order to check whether the microstructure is affected by building height, an EBSD map has been acquired at the top of a vertical specimen (*i.e.* far away from the building plate, see Figure 6).

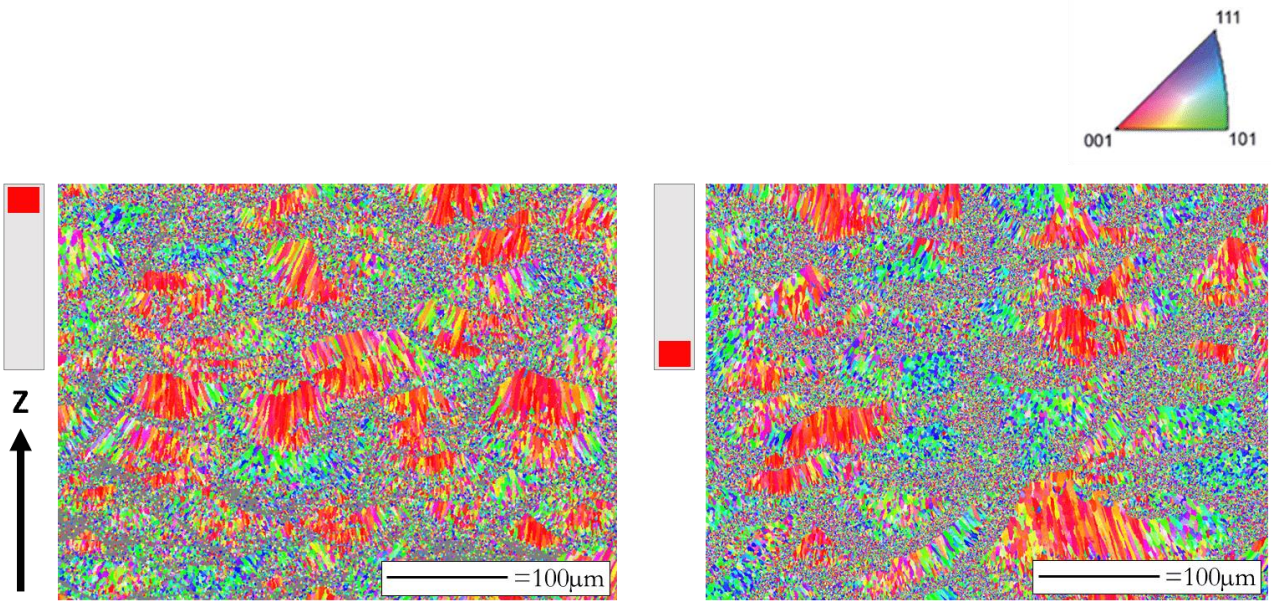


*Figure 6 : EBSD IPF-Z (Z: building direction) of the vertically 3D printed Al6061-$Zr_{1.2}$ (left) at the top of the traction specimen (right) at the bottom of the traction specimen (magnifications x250).*

In order to check whether the thermal history associated with building height could impact grain growth, an EBSD has been acquired at 5cm above the building plate (left). It reveals a similar duplex microstructure, showing that heat extraction in elongated samples did not impact the physics of the solidification process. A variation of thermal gradient along with the sample height could have impacted some microstructure aspects. In addition it can be argued that the bottom of the parts are subjected to repeated temperature cycles, leading in particular to a different precipitation behaviour. As a matter of fact, the picture acquired at the bottom of the tensile specimen seems to exhibit a higher fraction of recovered grains (*i.e.* textured according to [110] or [111]). However, the effect on macroscopic mechanical properties of such minor microstructural features differences is shown to be limited.

Overall, the similarity in terms of mechanical properties between virgin and recycled powders support the contention that dry coating allows to produce composite Al6061-YSZ particles able to withstand manipulation and recovery.

### 3.1.4 Charpy tests

Regarding toughness results, the first comment pertains to the good reproducibility (that is to say ±1J/cm²), which is again a sign of the good homogeneity of the 3D printed specimens at the macroscopic scale, and a tribute to the absence of cracks. The mean toughness is equal to 17J/cm². It is worth noting that these values are even better than results proposed in the literature for non 3D printed materials (for illustrative purpose : 12.8J/cm² with Al6061-$Si_3N_4$ [45]).

### 3.2 T6 heat treatment

A classic T6 HT has been applied to the horizontally 3D printed Al6061-$Zr_{1.2}$ alloy. For wrought Al6061 alloy, the solution annealing stage of the T6 HT aims at putting back Mg and Si elements in solid solution, in order to precipitate β'' phases during the following ageing HT. It should be emphasized that T6 HT does not appear adapted to extra-fine LBM microstructure. However, because of the strong growth kinetic dependence of β'', β' and $Mg_2Si$ phases with temperature, the issue of the multi pass and re-heating steps inherent to the LBM process on the precipitation of nano β'' during the ageing step is worth investigating.

#### 3.2.1 Microstructure

Figure 7 compares the microstructure of T6 HT Al6061-$Zr_{1.2}$ alloy with the as-built one. From a general standpoint, the duplex microstructure has partially disappeared and the majority of sub-micron equiaxed grains have been replaced by much bigger (say 10-50µm) ones. Remaining columnar grains are still in the same range of grain size and textured according to the [100] direction for those oriented parallel to the building direction. Such observation can be attributed to the Ostwald ripening mechanism [46]. Taking a characteristic value for the self-diffusion of Al in $\alpha_{Al}$ of the order of $10^{-12}$ -$10^{-13}$ m²/s at 800K [47], the $\alpha_{Al}$ phase can potentially growth over a distance of 20µm.

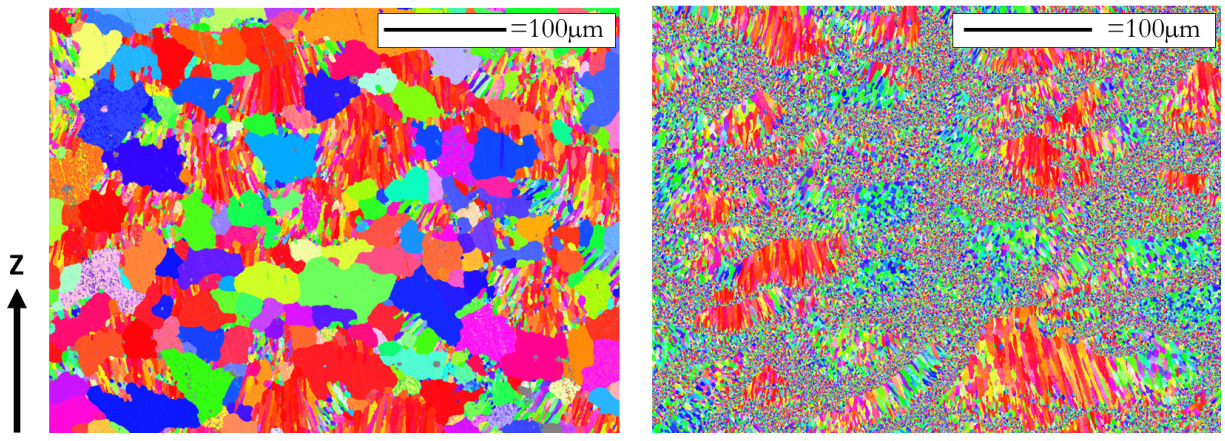


*Figure 7 : EBSD IPF-Z (Z: building direction) of the T6 HT 3D printed Al6061-$Zr_{1.2}$ alloy (left) compared to the as-built one (right) in YZ plane (magnifications x250).*

To restrict this grain growth, a T6' HT has been investigated. More precisely, the solution HT step is reduced from 5h to 15min. No significant improvement of the hardness response has been induced. EBSD acquisition revealed a quasi-equivalent grain growth compared to the T6 HT.

Back to the T6 HT microstructure, STEM EDX measurements taken inside one large equiaxed grain highlight a wide variety of precipitates. At the micronic scale, one can notice (Figure 8):

- (ZrSi) rich precipitates, with various forms and sizes (>20nm). It can be thought that the Si involved in these (ZrSi) phases will not be available and used for the formation of nano-β''. Indeed, an analysis of the formation enthalpies shows that many Si-Zr intermetallics are thermodynamically favoured in comparison to $Mg_2Si$ [48].

- Some small Mg/Si/Cu rich precipitates (≈10-20nm), possibly nucleated on (Zr,Si) particles.

- Mg/Al rich oxides (white arrows), known to act as heterogeneous nucleation sites for $Al_3Zr$ phases [15].

- Some Al/Cr/Fe/Si dispersoïds (≈50-100nm, blue arrows) classically encountered in T6 HT wrought Al6061 alloy [49].

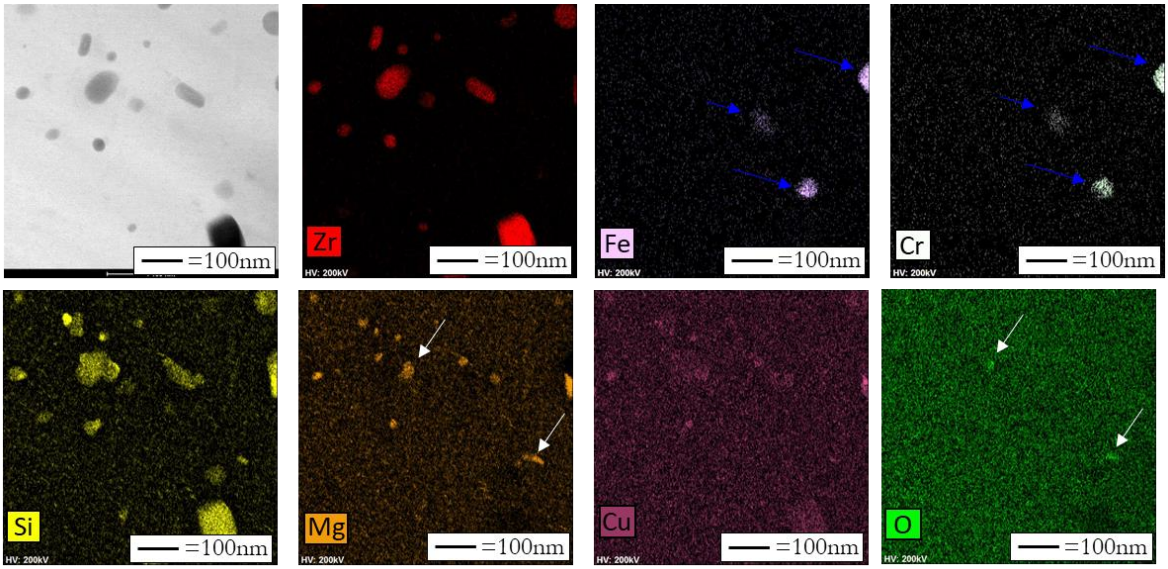


*Figure 8 : BF-TEM image and STEM-EDX maps of the micronic precipitates (>20nm) present inside a large equiaxed grain of the T6 HT Al6061-$Zr_{1.2}$ alloy showing Zr, Fe, Cr, Si, Mg, Cu and O elements.*

At the nanometric scale, classical β''-$Mg_xSi_y$ ([2,49,50]) precipitates are observed. Figure 9 shows the SAED pattern of the Al matrix oriented in [100] direction (left), with BF and DF images highlighting the presence of needle shaped phases with the main growth direction along $\langle 001 \rangle_{Al}$ (right). STEM-EDX maps of Mg and Si elements further confirmed the enrichment of Mg and Si near these elongated nano-phases. Only a fraction of the Si and Mg likely combines to form β'' hardening precipitates, the other fraction being used for Zr/Si precipitates or others. Their nano-size (roughly 25nm long and 5nm wide) will probably contribute to the engineering yield and ultimate strengths.

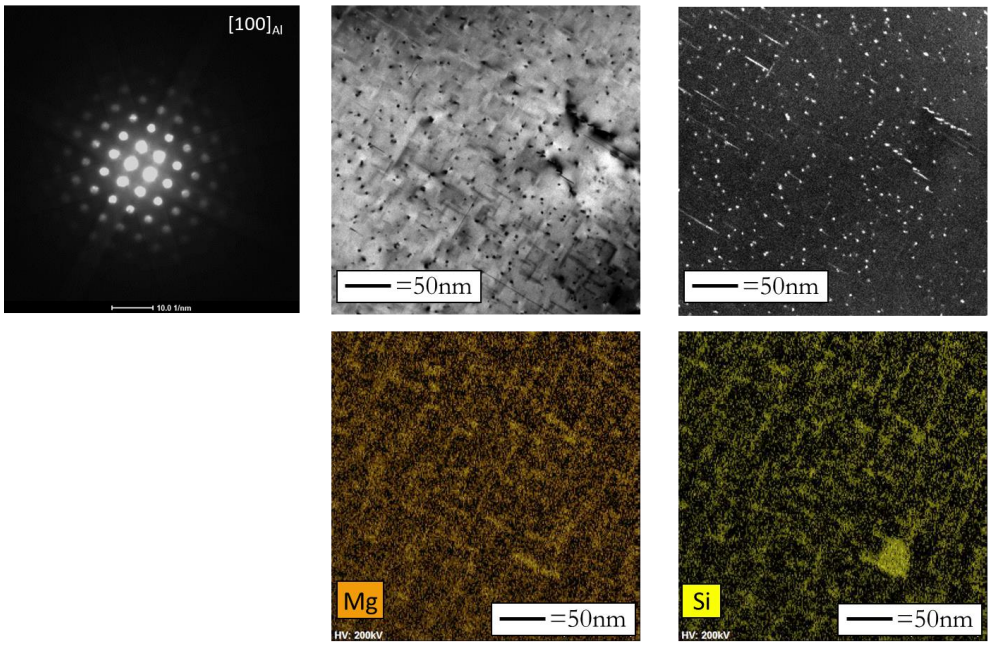


*Figure 9 : Nanoprecipitation in T6 HT Al6061-$Zr_{1.2}$.Diffraction pattern of the matrix in [100] direction with BF-TEM /DF-TEM images and STEM-EDX maps of the nano-β'' precipitates present inside a large equiaxed grain of the T6 3D printed Al6061-$Zr_{1.2}$ alloy showing Mg and Si elements.*

### 3.2.2 Micro-hardness

Table 2 compares the hardness response of the as-built Al6061-$Zr_{1.2}$ with the T6 HT Al6061-$Zr_{1.2}$ and the T6 HT wrought Al6061. The T6 HT significantly improves the hardness of the 3D printed Al6061-$Zr_{1.2}$ alloy (+38%). This can probably be attributed to the nucleation of nano-β'' particles. In addition, although a grain growth is noticed after the T6 HT, the grain size remains small compared to the T6 wrought Al6061 case.

| Wrought Al6061 | LBM Al6061-$Zr_{1.2}$ | T6 wrought Al6061 | T6 LBM Al6061-$Zr_{1.2}$ |
|---|---|---|---|
| 30 HV [41] | 90±2 HV | 95 HV [41] | 124±4 HV |

*Table 2 : Comparison of Vickers hardness response for LBM Al6061-$Zr_{1.2}$ states with wrought Al6061 ones.*

### 3.2.3 Tensile response

The additively manufactured Al6061-$Zr_{1.2}$ alloy has higher strength than the wrought one (bare product [4]). A slight increase of the engineering yield strength (from $\sigma_y$=276 MPa to $\sigma_y$=289 MPa) and the engineering ultimate strength (from $\sigma_{UTS}$=310 MPa to $\sigma_{UTS}$=330 MPa) is observed. This variation is, as expected to the detriment of the ductility (from 17% to 12.5%).

It is again worth noting that the reproducibility among the five tensile specimens tested is very good. The standard deviation remains small for the engineering yield and ultimate strengths (±4MPa) as for the ductility (±1%).

### 3.3 Adapted heat treatment

The as-built Al6061-$Zr_{1.2}$ microstructure is unique and significantly different from the wrought Al6061 case. The addition of Zr provides new opportunities to design specific adapted HT for the additively manufactured material. Therefore, three different ageing temperatures are investigated

(175°C, 300°C and 400°C) without solution annealing (Figure 10). The objective is also to avoid the grain growth inherent to the solution annealing step of the T6 HT.

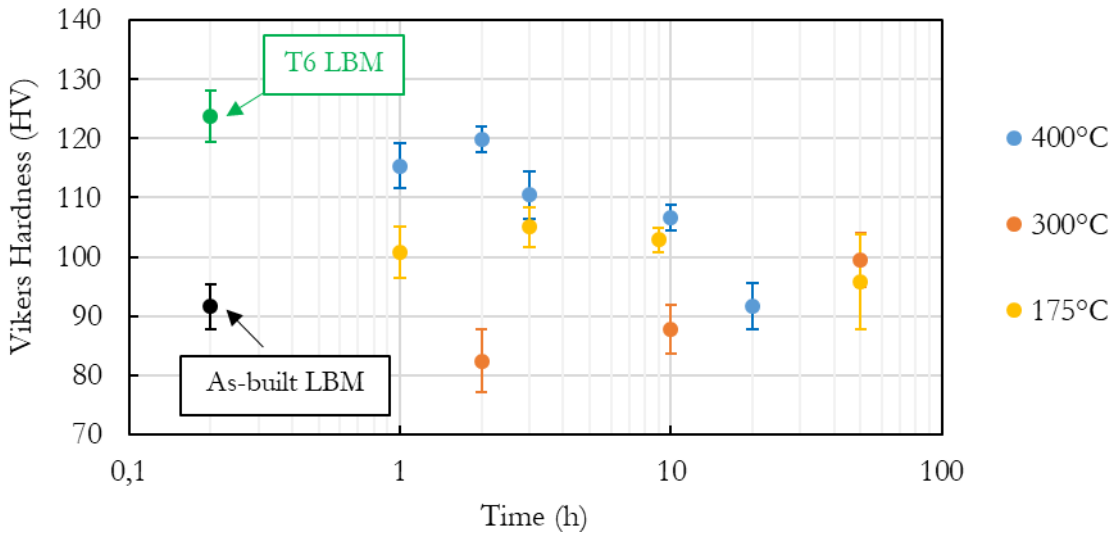


*Figure 10 : Evolution of the hardness of the as-built Al6061-$Zr_{1.2}$ heat treated at 175°C, 300°C and 400°C with ageing time (hours).*

### 3.3.1 Micro-hardness

Figure 10 sums up the hardness response for the three ageing temperatures. Two main features are underlined. First, for the 175°C and 400°C ageing temperatures, the hardness curve is going through a maximum hardness peak, this maximum depending upon temperature. Second, an absolute maximum hardness is achieved after 2H at 400°C, the value being equivalent to that of the T6 HT Al6061-$Zr_{1.2}$ state. This case is deeply investigated thereafter.

The 175°C curve exhibits a maximum hardness after 3 hours, increasing from 92 to 105 HV. From a general standpoint, such hardness evolution is classically observed during the heat treatment of Al-Si-Mg alloys at 180°C, and is attributed to β'' precipitation [50]. Nevertheless, in comparison, the T6 HT improved the response up to 122HV, although coarser grains were induced. One assumption is that the available fraction of Mg and Si in solid solution after printing and multiple rescanning is smaller compared to that after the solution HT combined with a quenching. Consequently, a restricted quantity of β'' can effectively precipitate, explaining the limited harness increase after 3 hours at 175°C. With increasing ageing time, β'' particles start to coarsen, becoming less hardening β'/β ($Mg_2Si$) phases [50]. Therefore, the hardness decreases (see Figure 10, 175°C data points). It is worth noting that such precipitation sequence has been widely studied [1,50] and is probably not affected by YSZ addition. The quantity of achievable β'' is even more restricted since 30-40% of the Mg evaporates during the LBM process (see Table 1). Therefore, these aspects should be directly taken into consideration in the powder gas atomisation step, through an Mg content higher than the norm, say by 30-40% for example. This is particularly true for the 6061 alloy where the amounts of Mg and Si have been specifically selected to promote the formation of hardening β'' phases. However, the principle can be extended to other elements with high partial pressure, e.g. Zn in the 7075 alloy.

The 300°C curve is quite difficult to understand. The hardness is deteriorated after 2 hours compared to the reference (as-built state), then it increases steadily and its peak is still not reached after 50 hours. Using background from wrought Al6061, such an ageing temperature (300°C) favours the rapid coarsening of β'' particles and consequently the precipitation of less-

hardening large β'/β phases [1]. Thereafter, the hardness of the Al6061-$Zr_{1.2}$ alloy gradually increases, possibly due to the precipitation of nano-$Al_3Zr$ phases. Clouet et al [51] have studied the nucleation kinetics of $Al_3Zr$ and $Al_3Sc$ in aluminium using cluster dynamics (Figure 11). At 300°C, the kinetic of $Al_3Sc$ growth (likely similar to the $Al_3Zr$ one) remains limited before $10^4$-$10^5$ (s) of ageing time (Figure 11), explaining the postponed hardness increase (compared to the 400°C ageing temperature, Figure 10).

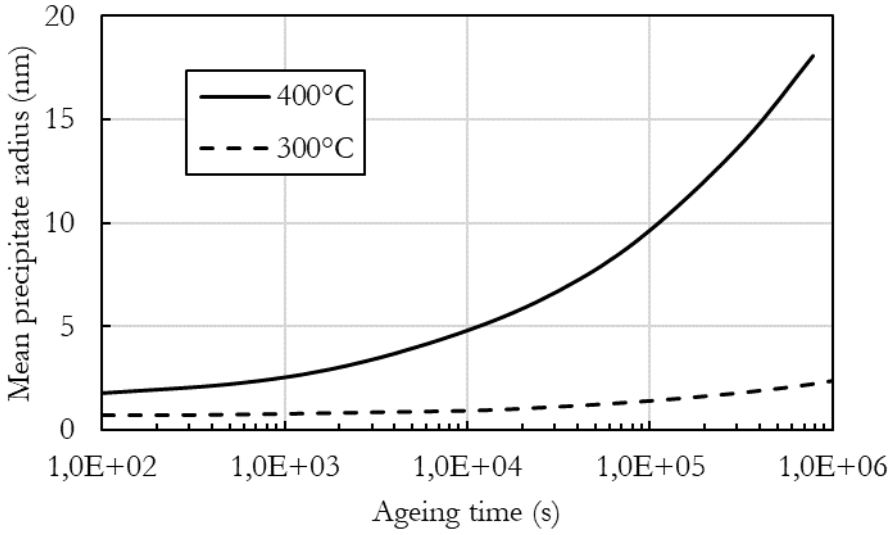


*Figure 11 : Mean $Al_3Sc$ precipitate radius with ageing time (seconds) for a solid solution of composition $x_{Sc}$=0.18at% at 300°C and 400°C, extracted from [51].*

The last curve to be treated is the 400°C. The hardness rapidly increases until 120HV after 2 hours. Then, the hardness decreases down to the as-built reference state after 20 hours of ageing. Reasons for such an evolution are discussed further on.

### 3.3.2 Focus on 400°C-2H case

Since the 400°C-2H HT exhibits the maximum hardness of this adapted HT study, its microstructure and mechanical response are deeply investigated.

#### 3.3.2.1 Microstructure

An EBSD acquisition reveals a duplex microstructure similar to the as-built Al6061-$Zr_{1.2}$ one, without any observable grain growth. It is worth noting that a similar behaviour (absence of grain growth) has been observed even after 20 hours at 400°C, meaning that this ageing temperature allows to keep the very fine microstructure.

To correlate macroscopic mechanical properties with microstructural features, a FIB lamella was prepared into a columnar region. In this specific region in the as-built material, a previous study has already shown that the Zr solute element is trapped in solid solution within the FCC $\alpha_{Al}$ matrix [15]. At low magnification, a wide variety of precipitates are present (Figure 12). Large (>300nm) Mg/Si rich particles (probably $Mg_2Si$) could have grown because of the high HT temperature [50]. In addition, as already noted, the Si element seems to combine with Zr. Last but not least, some Mg-based oxides (spinels) are still present, that supports their good temperature stability.

Using the KAM technique detailed in 3.1.1b), a quasi-identical mean angle of misorientation compared to the as-built state has been found. EBSD has been acquired with same magnification and pixel size, leading to a dislocation density again equal to $5x10^{14}m^{-2}$. However, it is relevant to mention that the intra-grain dislocation structure (forest dislocations) has been reduced after the 400°C-2H HT (compare Figure 4 and Figure 12). However, the annihilation of dislocations with opposite Burgers vectors will not change the overall misorientation, and as such will unfortunately not be detectable by the KAM technique.

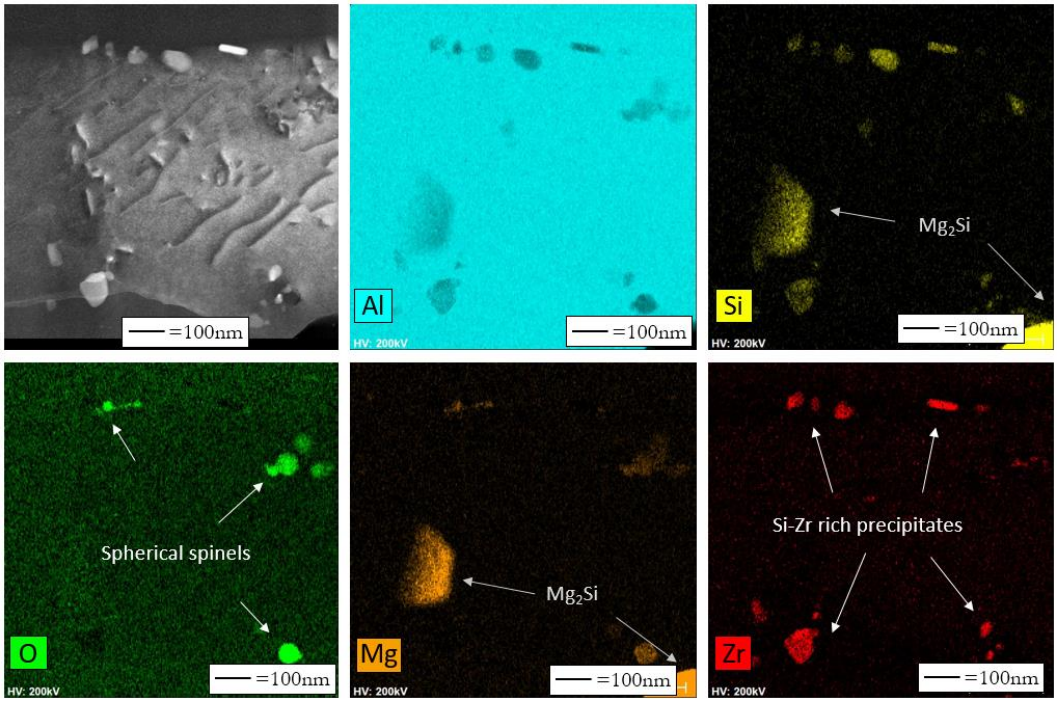


*Figure 12 : BF-TEM image and STEM-EDX maps inside a columnar grain of the HT (400°C-2H) 3D printed Al6061-$Zr_{1.2}$ showing Al, Si, O, Mg and Zr elements.*

At an even finer scale, nano particles are uniformly distributed in the matrix. Figure 13 presents a diffraction pattern of the FCC $\alpha_{Al}$ matrix in [100] direction (left). Superlattice spots located at a position 1/2 $d_{hkl}$ of Al matrix are observed. They are related to $Al_3Zr$ structure as already identified in [15]. The selection of these spots by a contrast aperture induces the dark field image of Figure 13.b. These nano-phases have a typical dimension around 2-3 nm and are coherent with the matrix as observed in the BF and HRTEM images of Figure 13.c and Figure 13.d. STEM-EDX maps of Zr and Al elements (Figure 13.e-g) further confirmed the nature of the nano-precipitates. It is widely documented that Al-Zr alloys can precipitate strengthening $L_{12}$ $Al_3Zr$ nano-particles during an additional aging heat treatment [52–55]. $Al_3Zr$ precipitates exhibit high thermal stability compared to the β'', as a result of the low impurity diffusion coefficient of Zr in solid Al ([56],[57]).This will result in better alloy temperature resistance thanks to grain growth and recrystallization inhibition [58–60]. The fact that the median size of these nano-$Al_3Zr$ particles is consistent with the theoretical prediction for the $Al_3Sc$ phase, *i.e.* roughly 3-4nm after 2H at 400°C (see Figure 11, [31]) should be emphasized. In addition, it should be stressed that no nano β'' precipitate is observed after such HT.

These $Al_3Zr$ precipitates probably keep growing upon further ageing at 400°C (see Figure 11), becoming less hardening. This trend can explain the gradual decrease of the hardness response after an optimized ageing time, *i.e.* 2 hours (Figure 10).

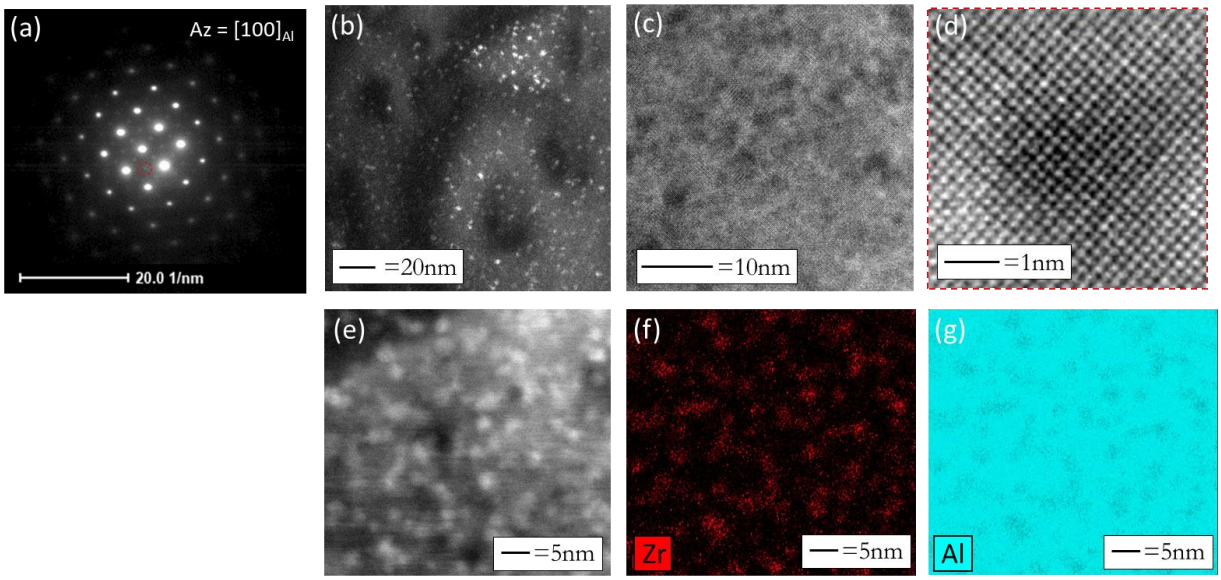


*Figure 13 : Nanoprecipitation in as-built Al6061-$Zr_{1.2}$ after 400°C-2H HT. Diffraction pattern of the $\alpha_{Al}$ matrix in [100] direction with BF-TEM and DF-TEM images and STEM-EDX maps of Zr and Al elements showing the nano-$Al_3Zr$ precipitates present inside a columnar grain of the HT (400°C-2H) 3D printed Al6061-$Zr_{1.2}$.*

### 3.3.2.2 Tensile properties

For this section, three tensile specimens have been horizontally 3D printed and heat treated (400°C-2H. Figure 14 shows the room-temperature engineering tensile curves of the as-built, T6 HT and 400°C-2H HT states of the Al6061-$Zr_{1.2}$ alloy. The 400°C-2H HT state displays the strongest strength response ($\sigma_y$=340MPa and $\sigma_{UTS}$=349MPa), and as a result the smallest elongation (≈11%). The unconventional curve shape of the 400°C-2H can be attributed to one or two Lüders bands propagation [24].

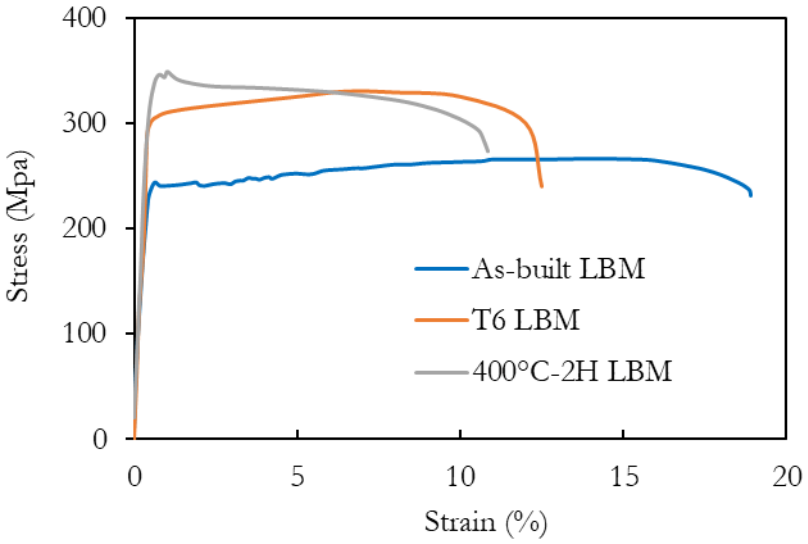


*Figure 14 : Room-temperature tensile curves of the as-built 3D printed Al6061-$Zr_{1.2}$ (blue curve), the T6 HT 3D printed Al6061-$Zr_{1.2}$ (orange curve), and the 400°C-2H HT 3D printed Al6061-$Zr_{1.2}$ (grey curve).*

As previously reported for other tensile tests, the standard deviation among the three tensile specimens tested after a 400°C-2H HT remains very small for the engineering yield and ultimate strengths (±1MPa), and limited for the ductility (±2%).

## 4. Discussion

The purpose of this section is first to propose plausible explanations of the high yield strength response of the as-built and HT 400°C-2H 3D printed Al6061-$Zr_{1.2}$ alloy. Second, the competitive precipitation phases of this particular alloy will be discussed. Last the different mechanical responses detailed in this paper are compared with the atomisation approach through the work of Mehta et al. [33] (Al6061+1wt%Zr).

### 4.1 An understanding of the FA modified Al6061 alloy hardening contributions

#### 4.1.1 Theoretical background

Yield stress is a combination of diverse strengthening contributions, and can be expressed as [61,62]:

$$\sigma_{YS} = \sigma_0 + \sigma_{gb} + \sigma_{ss} + \sqrt{{\sigma_{ps}}^2 + {\sigma_{ds}}^2} \quad \text{Eq. 2}$$

With,

- $\sigma_0$ the intrinsic matrix lattice resistance to dislocation motion, taken equal to 10MPa for aluminium [61,63].
- $\sigma_{gb}$ the grain boundary contribution (Hall-Petch law).
- $\sigma_{ss}$ the solid solution contribution.
- $\sigma_{ds}$ the dislocation contribution.
- $\sigma_{ps}$ the precipitates contribution.

a) Grain size contribution

The grain boundary contribution is deduced from the famous Hall Petch (HP) law [64,65]:

$$\sigma_{HP} = \frac{k}{\sqrt{d}} \quad \text{Eq. 3}$$

With *k* and *d* respectively a material constant and the grain size. For aluminium alloys, Thangaraju et al. [63] reported an HP constant of $k \approx 0.06 MPam^{1/2}$ over wide range of grain sizes (50nm-70µm).

b) Solid solution contribution

The strengthening solid solution contribution is calculated as [66]:

$$\sigma_{ss} = M \times 2^{1/3} \times \mu \times \left(\frac{\eta}{10}\right)^{4/3} \times c^{2/3} \quad \text{Eq. 4}$$

With *c* the weight fraction of the element in solid solution, *M* the Taylor factor, taken equal to 3.06 for FCC metals [67,68]. The shear modulus $\mu$ is calculated through the following equation:

$$\mu = \frac{E}{2\times(1+\xi)} \quad \text{Eq. 5}$$

With $\xi$ the Poisson coefficient (0.33 for Al6061, [69]) and $E$ the Young modulus deduced from one tensile curve (68.9GPa, close to the literature data for Al6061 [70]). $\eta$ represents the crystallographic misfit induced by Zr atoms (in the present framework), and can be expressed as [66]:

$$\eta = \frac{3}{c_{Zr}} \times \frac{da}{a} \quad \text{Eq. 6}$$

c) Dislocation contribution

The dislocation contribution is calculated as [39,61,67]:

$$\sigma_{ds} = M \times \alpha \times \mu \times b \times \sqrt{\rho_0} \quad \text{Eq. 7}$$

With $\alpha$ a geometrical factor, taken equal to 0.27 [61], and $\rho_0$ the dislocation density of the material.

d) Precipitation contribution

The last possible contribution is the precipitation hardening. In view of the expected limited effect of large Mg-Si, Y-rich or dispersoïds precipitates, only $Al_3Zr$ precipitates are considered here. As a reminder, 100nm squared particles are present in equiaxed grains in the as-built state. 2nm nano-$Al_3Zr$ are formed during subsequent 400°C-2H HT in columnar zones. Two phenomena are widely described in the literature. Dislocations can either shear particles, or bow around when precipitates are strong enough to resist dislocation penetration (Orowan mechanism). The precipitation hardening mechanism mainly depends on the particle radius. The critical radius separating both regimes (at which maximal strengthening occurs) can be expressed as [66]:

$$R_c = \sqrt{\frac{3}{2}} \times \frac{\Gamma}{\gamma_{APB}} \times (1 + 1.5 \times \sqrt{\frac{f}{\pi}}) \quad \text{Eq. 8}$$

With $\Gamma$ the line tension ($\mu b^2/2$), $\gamma_{APB}$ the antiphase boundary energy for the $Al_3Zr$ shearing (namely 0.445J/m², see [71]) and $f$ the volumetric fraction of $Al_3Zr$ particles, equal to 0.9vol% and deduced from the following equation:

$$f = \frac{c_{Al3Zr}}{c_{Al3Zr} + \frac{\rho_{Al3Zr}}{\rho_{Al}} \times (1 - c_{Al3Zr})} \quad \text{Eq. 9}$$

With $c_{Al3Zr}$ the weight fraction of $Al_3Zr$. The estimated critical radius reaches 3.2nm. When particles are bigger than roughly 4nm, Orowan mechanism has to be considered. For low volumic fractions, the precipitate contribution can be deduced from [61]:

$$\sigma_{ps} = M \times 0.5 \times \frac{\mu \times b}{\sqrt{\pi}} \times \sqrt{f} \times \frac{1}{R} \quad \text{Eq. 10}$$

For the shearing mechanism, various contributions are documented in the literature:

- modulus mismatch ($\Delta\sigma_{mod}$) and coherency ($\Delta\sigma_{coh}$) strengthening when the dislocations are close to the $Al_3Zr$ precipitate.
- ordering ($\Delta\sigma_{ord}$) strengthening when the dislocations have sheared the $L1_2$ $Al_3Zr$ precipitates.

Zhou et al. [42] have proposed that in the 1-4nm size range, order strengthening is predominant for $Al_3Zr$ nano-precipitates and can be expressed as [42,67,72]:

$$\sigma_{ps} = 0.81 \times M \times \frac{\gamma_{APB}}{2b} \times \sqrt{\frac{3\pi f}{8}} \quad \text{Eq. 11}$$

### 4.1.2 As-built state

The observed difference between the horizontally and vertically built samples can be explained either by the mean grain size according to the loading direction (see 3.1.1 a) and [73]), or by the orientation of the defects [73]. As an homogeneous repartition of spherical pores has been previously highlighted [15], it is here considered that the mean grain size (depending on the loading direction) is the major contribution to explain the observed yield strength difference. Using results detailed in 3.1.1a, the HP contribution (Eq. 1) amounts to 64MPa for horizontal specimens, against 34MPa for vertical specimens. Although a smaller difference (namely 20MPa) is experimentally observed, these values are in good order of magnitude agreement. The difference can be possibly due to the assumption made in section 3.1.1a)) to calculate the mean grain dimension. In reality, all the columnar grains are not oriented along the Z direction, only a fraction of them are. Consequently, the HP contribution is rather overestimated for horizontal specimens and underestimated for vertical ones. In any case, in comparison with the experimental values, these results suggest that other strengthening contributions should have a significantly higher effect.

Regarding the solid solution strengthening, the columnar grain fraction being roughly 50%, it is assumed that half of the total Zr content is trapped into solid solution in these regions (*i.e.* 0.6wt%). The $\eta$ parameter is calculated using EVA software and XRD acquisitions (Eq. 6). The lattice parameters of pure Al6061 and Al6061-$Zr_{1.2}$ are compared to determine the mismatch induced by YSZ addition. A 0.03% misfit is measured. Consequently, the calculated solid solution contribution (Eq. 4) related to the 0.6wt% of Zr reaches 12MPa. It should be stressed that a fraction of other elements (Mg/Si) are probably in solid solution, but their contribution to the yield strength is not calculated in this paper. In any case, it can be safely stated that solid solution strengthening is not the dominant hardening mechanism.

For the as-built state, the dislocation density has been estimated equal to $5x10^{14}m^{-2}$ (see 3.1.1b). Using this value, Taylor's equation (Eq. 7) gives an estimate of 130MPa for the effective dislocation contribution, confirming the major importance of these crystallographic defects.

In the as built state, $Al_3Zr$ precipitates are only present in equiaxed zones, with cubic-like shapes and dimensions in the 50-100nm size range [15], meaning that the Orowan mechanism has to be considered. Using Eq. 10 the precipitation hardening reaches 12MPa.

Table 3 sums up the calculated contributions. Even though the refined grain microstructure contributes significantly to the yield strength of the as-built Al6061-$Zr_{1.2}$, calculations revealed that dislocations constitute the most important hardening contribution. These two aspects mainly explained the strong improvement in comparison with wrought 6061 alloy. The theoretical yield strength is found to lie in the range from 187MPa to 217MPa, which is slightly lower than the experimental one. However, the results remain comparable, and it should be recalled that not all elements in solid solution and all precipitates have been included in the estimation of the yield strength, and that the measured dislocation density does not include forest dislocations.

### 4.1.3 400°C-2H state

The 400°C HT features have been described in section 3.3.2. The grain size remains unchanged, so is the HP contribution (*i.e.* 64MPa). It will be assumed that the Zr content trapped into solid solution in columnar region in the as-built state has henceforth been used to precipitate nano-$L1_2$ $Al_3Zr$ particles. As a result, the solid solution contribution is not anymore included in the theoretical yield strength. It has been demonstrated that the shearing mechanism is appropriate for the 2nm-$L1_2$ ordered $Al_3Zr$ strengthening from the columnar regions. Using Eq. 11, the order strengthening contribution related to the nano-$Al_3Zr$ reaches 198MPa. The dislocation contribution remains unchanged (see 3.3.2.1). Table 3 sums up the calculated contributions.

| | $\sigma_0$ | $\sigma_{HP}$ | $\sigma_{ds}$ | $\sigma_{ps}$ | $\sigma_{YS\ (theoretical)}$ | $\sigma_{YS\ (experimental)}$ |
|---|---|---|---|---|---|---|
| As built | 10 | 34-64 | 12 | 130 | 12 | 187-217 |
| 400°C-2H | 10 | 64 | 130 | 198 | 310 | 340 |

*Table 3 : Summary of the four calculated contributions to the theoretical yield strength of the as-built and 400°C-2H 3D printed Al6061-$Zr_{1.2}$ alloy.*

The obtained theoretical value is similar, although again somewhat smaller, compared to the experimental data. As mentioned above, not all precipitates have been taken into account for the yield strength calculations, which could explain the discrepancy. For this HT state, the nano-$Al_3Zr$ precipitates and the high dislocation density are the dominant contributions. Nevertheless, it is worth noting that the precipitation's contribution (198 MPa) of nanosized Al3Zr precipitates may be overestimated. Indeed, it has been somewhat arbitrarily considered that every Zr atoms trapped in solid solution in the as-built state reacts during the 400°C-2H heat treatment to form these hardening phases, a fact we have no evidence. However, without deeper investigations (APT measurements for example), the exact nanosized Al3Zr precipitates concentration cannot be safely established.

## 4.2 Competitive phases precipitations of this particular alloy and adapted heat treatment

This study raises some interesting issues regarding the mechanical response of a 3D printed Al6061 modified alloy. First, one could have expected that the LBM conditions promote the trapping into solid solution of the alloying elements. This assumption is likely valid for one single pass. Indeed, cooling rate encountered during the process (say from $10^5$ to $10^7$K/s, [74,75]) is very high, leaving only limited time for particles precipitation. However, in view of the multi-pass rescanning inherent to the 3D process principle, it appears reasonable to invoke in-situ ageing to explain the observed large MgSi precipitates present in the as-built state. This statement is particularly true for alloys containing elements which precipitate at low temperature (Mg-Si based precipitates for example).

The classic solution HT from wrought alloys practice can address this challenge. However, three points need to be raised. First, the high temperature of the solution HT step promotes grain growth and partially removes the extra fine microstructure induce by 3D printing rapid solidification. Second, as earlier mentioned, a major contribution for the 6061-$Zr_{1.2}$ is the dislocation density, probably in part reduced during high temperature HT. Third, the YSZ addition further complicates the understanding. In fact, as detailed in 3.2.1, some large Zr-Si rich particles likely precipitate during the solution HT step, reducing the amount of Si available for β'' precipitation during subsequent ageing. In this context, the classic solution HT temperature is likely not fully adapted to the 3D printing specifically design Al6061-$Zr_{1.2}$ alloy, as well as the ageing time of the T6 HT.

The last tricky issue, again arising from YSZ addition, is the combination of multiple thermal growth kinetics dependence for the precipitation of hardening nano-particles. In fact one should understand the increase of engineering yield and ultimate strengths for T6 and 400°C-2H HTs as mainly due to nano-precipitates hardening. The challenge regards two kinds of precipitates chemically different (β'' and $Al_3Zr$) with strongly different growth kinetic in terms of temperature. This can be linked to the high impurity diffusion coefficients of Mg and Si as compared to Zr in $\alpha_{Al}$[57]. Consequently, at 400°C, β'' particles very rapidly evolve into non-hardening $Mg_2Si$ phases. On the other hand, the 175°C temperature (appropriate for β'' precipitation) is much too low to expect significant nano-$Al_3Zr$ precipitation. Figure 15 summarizes the proposed precipitation sequences of the HT 3D printed Al6061-$Zr_{1.2}$ for the three investigated ageing temperatures.

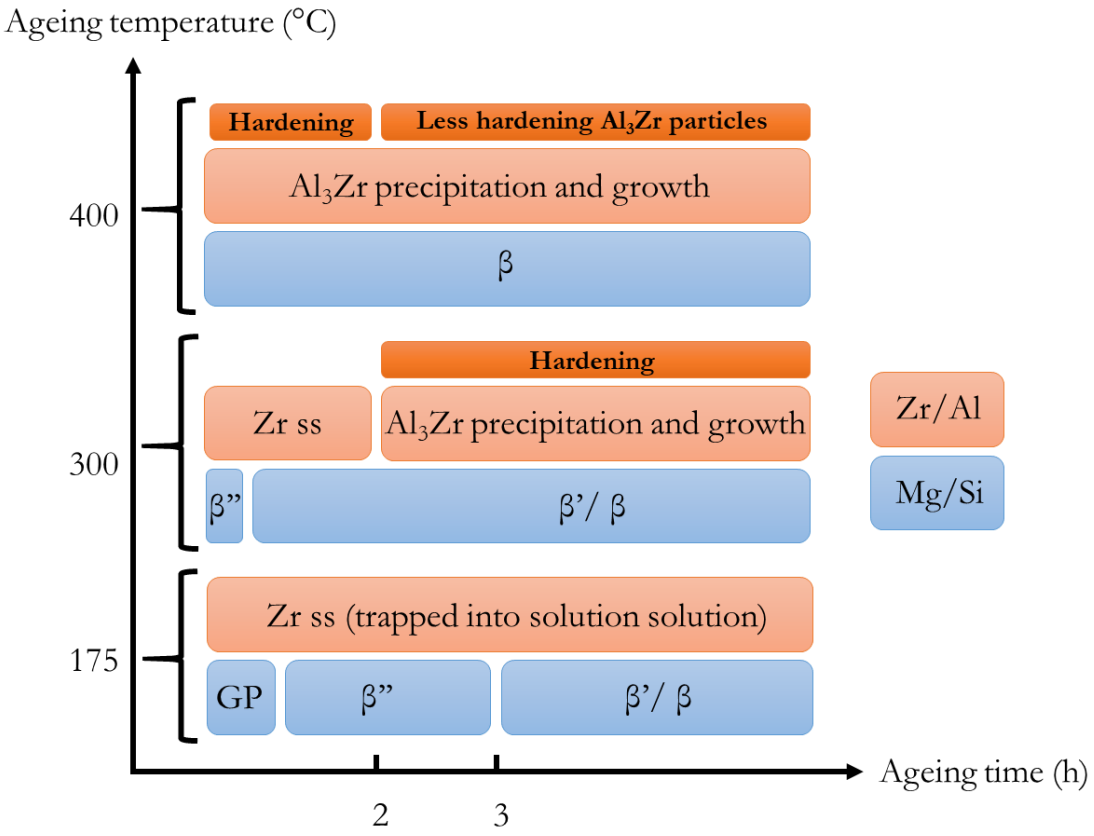


*Figure 15 : Summary of the proposed precipitation sequences of the HT 3D printed Al6061-Zr1.2 (for three ageing temperatures).*

## 4.3 Overview

Table 4 proposes a comparison of the mechanical response for several states of the Al6061-$Zr_{1.2}$ alloy with standard wrought 6061 and data from the work of Mehta et al. [33]. As illustrated, a wide variety of mechanical properties can be achieved (say from 241 to 349 MPa for the yield strength and from 11 to 17% for the ductility). The alloy achieves higher engineering yield and ultimate strengths than the wrought Al6061 alloy. In addition, a quasi-isotropic microstructure has been 3D printed, with good mechanical response reproducibility. Finally, although chemical compositions are not *stricto sensu* equal, mechanical properties are close to those of Mehta et al., which supports the validity of the mixing approach to develop new alloys. In order to avoid several atomisation, this method allows to screen a wide chemical compositions panel to find the optimized balance between hot cracking susceptibility and mechanical properties.

| | $\sigma_y$ | $\sigma_{UTS}$ | $\varepsilon$ |
|---|---|---|---|
| Wrought Al6061 [41] | 55 | 124 | 25 |
| As-built Al6061-$Zr_{1.2}$ (mixing) | 241 | 266 | 17 |
| As-built Al6061-$Zr_1$ [33] (atomisation) | 210 | 268 | 26.5 |
| T6 wrought Al6061 [41] | 276 | 310 | 17 |
| T6 HT Al6061-$Zr_{1.2}$ (mixing) | 289 | 330 | 12.5 |
| T6 HT Al6061-$Zr_1$ (atomisation) | 300 | 327 | 13.9 |
| 400°C-2H HT Al6061-$Zr_{1.2}$ | 340 | 349 | 11 |

*Table 4 : Comparison of mechanical response for several state of the Al6061-$Zr_{1.2}$ with classics wrought 6061 ones [41] and Mehta et al. work [33].*

## 5. Conclusion

A novel crack free modified 6061 aluminium alloy was 3D printed using a coated gas atomized Al6061 powder with 2 volumic % of YSZ particles. The mechanical response of this developed Al6061-$Zr_{1.2}$ alloy has been studied. Based on the results presented through this paper, the following conclusions arise:

- A quasi-isotropic behaviour is consistent with the duplex equiaxed-columnar grain microstructure. In addition, the use of recycled powder does not impact tensile properties, a key aspect in view of the reduction of material waste.
- For the as-built state, the alloy exhibits higher yield and ultimate strengths compared to wrought Al6061. This could mainly be attributed to a very large dislocation density and an extra-fine grain microstructure.
- A T6 heat treatment, including both solution hardening at 530°C for 5 hours, quench into water, and ageing at 175°C for 9 hours increased the as-built 3D printed Al6061-$Zr_{1.2}$ yield

and ultimate strengths. A significant grain growth and the precipitation of classical nano β''-$Mg_xSi_y$ particles have been evidenced.

- To avoid grain growth and take advantage of the Zr content trapped into solid solution after LBM processing, several annealing strategies have been investigated. Such an approach enabled to further increase the yield and ultimate strengths of this alloy. Micro-Vickers hardness measurements highlighted a maximum peak after 2 hours at 400°C, with strong yield and ultimate strengths of respectively $\sigma_Y$=340MPa and $\sigma_{UTS}$=349MPa. This improvement has been attributed to ordered $L1_2$ $Al_3Zr$ nanoprecipitation, from remaining Zr content trapped in solid solution in the as-built state.
- The study highlighted that it is difficult to control the coordinate precipitation of hardening nanoparticles ($Al_3Zr$ and β'') with different thermal growth kinetics.

To conclude, the mechanical properties of this additively manufactured modified A6061 alloy have showed promising results, supporting the YSZ addition approach to solve the hot cracking issues for hot cracking prone aluminium alloys during laser beam melting. However, the work could be extended. Al6061-$Zr_{1.2}$ thermal and corrosion properties could be investigated. In a more complete approach, the partial evaporation of the Mg content during the 3D printing process should be anticipated during the atomisation step, otherwise benefit of β'' hardening phases will be restricted. Such contention is valid for all high partial pressure elements used to precipitate nano-hardening phases in wrought aluminium alloys.

Acknowledgements

The TEM pictures were acquired at the CEA NanoCharacterization Platform (PFNC) - Minatec, thanks to the French RTB (IRT Nanoelec) and the equipex NanoID. The authors thanks Nathalie LADRAT for FIB lamella preparation. Céline RIBIERE is also acknowledged for her 3D printing technical assistance. M.O thanks Florian PEYROUZET for fruitful discussions.

[1] C.F. Tan, M.R. Said, Effect of Hardness Test on Precipitation Hardening Aluminium Alloy 6061-T6, Chiang Mai J Sci. (2009) 12.
[2] H. Li, Characterizations of precipitation behavior of Al-Mg-Si alloys under different heat treatments, CHINA FOUNDRY. 15 (2018).
[3] A.K. Gupta, D.J. Lloyd, S.A. Court, Precipitation hardening in Al–Mg–Si alloys with and without excess Si, Mater. Sci. Eng. A. 316 (2001) 11–17. https://doi.org/10.1016/S0921-5093(01)01247-3.
[4] S.J. Andersen, H.W. Zandbergen, J. Jansen, C. TRáHOLT, U. Tundal, O. Reiso, The crystal structure of the B'' phase in Al-Mg-Si alloys, (1998) 16.
[5] Andersen, S.J., C.D. Marioara, R. Vissers, A. Frøseth, H.W. Zandbergen, The structural relation between precipitates in Al–Mg–Si alloys, the Al-matrix and diamond silicon, with emphasis on the trigonal phase U1-MgAl2Si2, Mater. Sci. Eng. A. 444 (2007) 157–169. https://doi.org/10.1016/j.msea.2006.08.084.
[6] Andersen, S.J., C.D. Marioara, A. Frøseth, R. Vissers, H.W. Zandbergen, Crystal structure of the orthorhombic U2-Al4Mg4Si4 precipitate in the Al–Mg–Si alloy system and its relation to the β′ and β″ phases, Mater. Sci. Eng. A. 390 (2005) 127–138. https://doi.org/10.1016/j.msea.2004.09.019.
[7] R. Vissers, M.A. van Huis, J. Jansen, H.W. Zandbergen, C.D. Marioara, S.J. Andersen, The crystal structure of the β′ phase in Al–Mg–Si alloys, Acta Mater. 55 (2007) 3815–3823. https://doi.org/10.1016/j.actamat.2007.02.032.
[8] N.T. Aboulkhair, M. Simonelli, L. Parry, I. Ashcroft, C. Tuck, R. Hague, 3D printing of Aluminium alloys: Additive Manufacturing of Aluminium alloys using selective laser melting, Prog. Mater. Sci. 106 (2019) 100578. https://doi.org/10.1016/j.pmatsci.2019.100578.
[9] D. Jafari, W.W. Wits, The utilization of selective laser melting technology on heat transfer devices for thermal energy conversion applications: A review, Renew. Sustain. Energy Rev. 91 (2018) 420–442. https://doi.org/10.1016/j.rser.2018.03.109.
[10] L. Thijs, K. Kempen, J.-P. Kruth, J. Van Humbeeck, Fine-structured aluminium products with controllable texture by selective laser melting of pre-alloyed AlSi10Mg powder, Acta Mater. 61 (2013) 1809–1819. https://doi.org/10.1016/j.actamat.2012.11.052.
[11] T. Kimura, T. Nakamoto, Microstructures and mechanical properties of A356 (AlSi7Mg0.3) aluminum alloy fabricated by selective laser melting, Mater. Des. 89 (2016) 1294–1301. https://doi.org/10.1016/j.matdes.2015.10.065.
[12] A. Aversa, G. Marchese, A. Saboori, E. Bassini, D. Manfredi, S. Biamino, D. Ugues, P. Fino, M. Lombardi, New Aluminum Alloys Specifically Designed for Laser Powder Bed Fusion: A Review, Materials. 12 (2019) 1007. https://doi.org/10.3390/ma12071007.
[13] M.L. Montero-Sistiaga, R. Mertens, B. Vrancken, X. Wang, B. Van Hooreweder, J.-P. Kruth, J. Van Humbeeck, Changing the alloy composition of Al7075 for better processability byselective laser melting, J. Mater. Process. Technol. 238 (2016) 437–445.
[14] J.H. Martin, B.D. Yahata, J.M. Hundley, J.A. Mayer, T.A. Schaedler, T.M. Pollock, 3D printing of high-strength aluminium alloys, Nature. 549 (2017) 365–369.
[15] M. Opprecht, J.-P. Garandet, G. Roux, C. Flament, M. Soulier, A solution to the hot cracking problem for aluminium alloys manufactured by laser beam melting, Acta Mater. 197 (2020) 40–53. https://doi.org/10.1016/j.actamat.2020.07.015.
[16] A. Sonawane, G. Roux, J.-J. Blandin, A. Despres, G. Martin, Cracking mechanism and its sensitivity to processing conditions during laser powder bed fusion of a structural aluminum alloy, Materialia. 15 (2021) 100976. https://doi.org/10.1016/j.mtla.2020.100976.
[17] H. Hyer, L. Zhou, A. Mehta, Y. Sohn, Effects of Alloy Composition and Solid-State Diffusion Kinetics on Powder Bed Fusion Cracking Susceptibility, J. Phase Equilibria Diffus. 42 (2021) 5–13. https://doi.org/10.1007/s11669-020-00844-y.
[18] H. Hyer, L. Zhou, A. Mehta, S. Park, T. Huynh, S. Song, Y. Bai, K. Cho, B. McWilliams, Y. Sohn, Composition-dependent solidification cracking of aluminum-silicon alloys during laser powder bed fusion, Acta Mater. 208 (2021) 116698. https://doi.org/10.1016/j.actamat.2021.116698.
[19] A.R. Zulhishamuddin, S.N. Aqida, M. Mohd Rashidi, A comparative study on wear behaviour of Cr/Mo surface modified grey cast iron, Opt. Laser Technol. 104 (2018) 164–169. https://doi.org/10.1016/j.optlastec.2018.02.027.

[20] S. Griffiths, M.D. Rossell, J. Croteau, N.Q. Vo, D.C. Dunand, C. Leinenbach, Effect of laser rescanning on the grain microstructure of a selective laser melted Al-Mg-Zr alloy, Mater. Charact. 143 (2018) 34–42. https://doi.org/10.1016/j.matchar.2018.03.033.
[21] M. Awd, J. Tenkamp, M. Hirtler, S. Siddique, M. Bambach, F. Walther, Comparison of Microstructure and Mechanical Properties of Scalmalloy® Produced by Selective Laser Melting and Laser Metal Deposition, Materials. 11 (2017) 17. https://doi.org/10.3390/ma11010017.
[22] D. Koutny, D. Palousek, L. Pantelejev, C. Hoeller, R. Pichler, L. Tesicky, J. Kaiser, Influence of Scanning Strategies on Processing of Aluminum Alloy EN AW 2618 Using Selective Laser Melting, Materials. 11 (2018) 298. https://doi.org/10.3390/ma11020298.
[23] Q. Jia, P. Rometsch, S. Cao, K. Zhang, X. Wu, Towards a high strength aluminium alloy development methodology for selective laser melting, Mater. Des. 174 (2019) 107775.
[24] Q. Jia, P. Rometsch, P. Kürnsteiner, Q. Chao, A. Huang, M. Weyland, L. Bourgeois, X. Wu, Selective laser melting of a high strength Al Mn Sc alloy: Alloy design and strengthening mechanisms, Acta Mater. 171 (2019) 108–118.
[25] E.A. Jägle, Z. Sheng, L. Wu, L. Lu, J. Risse, A. Weisheit, D. Raabe, Precipitation Reactions in Age-Hardenable Alloys During Laser Additive Manufacturing, JOM. 68 (2016) 943–949. https://doi.org/10.1007/s11837-015-1764-2.
[26] R. Li, H. Chen, C. Chen, H. Zhu, M. Wang, T. Yuan, B. Song, Selective Laser Melting of Gas Atomized Al–3.02Mg–0.2Sc–0.1Zr Alloy Powder: Microstructure and Mechanical Properties, Adv. Eng. Mater. 21 (2019) 1800650. https://doi.org/10.1002/adem.201800650.
[27] N.V. Dynin, V.V. Antipov, D.V. Khasikov, I. Benarieb, A.V. Zavodov, A.G. Evgenov, Structure and mechanical properties of an advanced aluminium alloy AlSi10MgCu(Ce,Zr) produced by selective laser melting, Mater. Lett. 284 (2021) 128898. https://doi.org/10.1016/j.matlet.2020.128898.
[28] L. Zhou, H. Hyer, J. Chang, A. Mehta, T. Huynh, Y. Yang, Y. Sohn, Microstructure, mechanical performance, and corrosion behavior of additively manufactured aluminum alloy 5083 with 0.7 and 1.0 wt% Zr addition, Mater. Sci. Eng. A. 823 (2021) 141679. https://doi.org/10.1016/j.msea.2021.141679.
[29] H. Hyer, L. Zhou, S. Park, T. Huynh, A. Mehta, S. Thapliyal, R.S. Mishra, Y. Sohn, Elimination of extraordinarily high cracking susceptibility of aluminum alloy fabricated by laser powder bed fusion, J. Mater. Sci. Technol. 103 (2022) 50–58. https://doi.org/10.1016/j.jmst.2021.06.023.
[30] J. Zhang, J. Gao, B. Song, L. Zhang, C. Han, C. Cai, K. Zhou, Y. Shi, A novel crack-free Ti-modified Al-Cu-Mg alloy designed for selective laser melting, Addit. Manuf. 38 (2021) 101829. https://doi.org/10.1016/j.addma.2020.101829.
[31] Q. Tan, J. Zhang, Q. Sun, Z. Fan, G. Li, Y. Yin, Y. Liu, M.-X. Zhang, Inoculation treatment of an additively manufactured 2024 aluminium alloy with titanium nanoparticles, Acta Mater. 196 (2020) 1–16. https://doi.org/10.1016/j.actamat.2020.06.026.
[32] M. Opprecht, J.-P. Garandet, G. Roux, C. Flament, An understanding of duplex microstructures encountered during high strength aluminium alloy laser beam melting processing, Acta Mater. 215 (2021) 117024. https://doi.org/10.1016/j.actamat.2021.117024.
[33] A. Mehta, L. Zhou, T. Huynh, S. Park, H. Hyer, S. Song, Y. Bai, D.D. Imholte, N.E. Woolstenhulme, D.M. Wachs, Y. Sohn, Additive manufacturing and mechanical properties of the dense and crack free Zr-modified aluminum alloy 6061 fabricated by the laser-powder bed fusion, Addit. Manuf. 41 (2021) 101966. https://doi.org/10.1016/j.addma.2021.101966.
[34] F. Wang, D. Qiu, Z. Liu, J. Taylor, M. Easton, M. Zhang, Crystallographic study of Al3Zr and Al3Nb as grain refiners for Al alloys, Trans. Nonferrous Met. Soc. China. 24 (2014) 2034–2040.
[35] L.-P. Lapierre-Boire, C. Blais, S. Pelletier, F. Chagnon, Improvement of flow of an iron-copper-graphite powder mix through additions of nanoparticles, Powder Technol. 299 (2016) 156–167. https://doi.org/10.1016/j.powtec.2016.05.046.
[36] J. Yang, A. Sliva, A. Banerjee, R.N. Dave, R. Pfeffer, Dry particle coating for improving the flowability of cohesive powders, Powder Technol. (2005) 13.
[37] C. Weingarten, D. Buchbinder, N. Pirch, W. Meiners, K. Wissenbach, R. Poprawe, Formation and reduction of hydrogen porosity during selective laser melting of AlSi10Mg, J. Mater. Process. Technol. 221 (2015) 112–120. https://doi.org/10.1016/j.jmatprotec.2015.02.013.

[38] C. Fressengeas, B. Beausir, C. Kerisit, A.-L. Helbert, T. Baudin, F. Brisset, M.-H. Mathon, R. Besnard, N. Bozzolo, On the evaluation of dislocation densities in pure tantalum from EBSD orientation data, Matér. Tech. 106 (2018) 604. https://doi.org/10.1051/mattech/2018058.
[39] F. Peyrouzet, D. Hachet, R. Soulas, C. Navone, S. Godet, S. Gorsse, Selective Laser Melting of Al0.3CoCrFeNi High-Entropy Alloy: Printability, Microstructure, and Mechanical Properties, JOM. 71 (2019) 3443–3451. https://doi.org/10.1007/s11837-019-03715-1.
[40] Y.J. Yin, J.Q. Sun, J. Guo, X.F. Kan, D.C. Yang, Mechanism of high yield strength and yield ratio of 316 L stainless steel by additive manufacturing, Mater. Sci. Eng. A. 744 (2019) 773–777. https://doi.org/10.1016/j.msea.2018.12.092.
[41] ASM Handbook, 10th ed., 1995.
[42] L. Zhou, H. Hyer, S. Park, H. Pan, Y. Bai, K.P. Rice, Y. Sohn, Microstructure and mechanical properties of Zr-modified aluminum alloy 5083 manufactured by laser powder bed fusion, Addit. Manuf. 28 (2019) 485–496. https://doi.org/10.1016/j.addma.2019.05.027.
[43] B. Reyne, P.-Y. Manach, N. Moës, Macroscopic consequences of Piobert–Lüders and Portevin–Le Chatelier bands during tensile deformation in Al-Mg alloys, Mater. Sci. Eng. A. 746 (2019) 187–196. https://doi.org/10.1016/j.msea.2019.01.009.
[44] Y. Zhao, J. Liu, T.D. Topping, E.J. Lavernia, Precipitation and aging phenomena in an ultrafine grained Al-Zn alloy by severe plastic deformation, J. Alloys Compd. 851 (2021) 156931. https://doi.org/10.1016/j.jallcom.2020.156931.
[45] T.V. Kumar, M. Indu, A.S. Gopal, A.V. Krishna, D.V. Reddy, Microstructure Study and Mechanical Testing of Al 6061-Si3n4 Metal Matrix Composites, Met. Matrix Compos. 8 (2019) 5.
[46] H. Mohammadi, A.R. Eivani, S.H. Seyedein, M. Ghosh, Modified Monte Carlo approach for simulation of grain growth and Ostwald ripening in two-phase Zn–22Al alloy, J. Mater. Res. Technol. 9 (2020) 9620–9631. https://doi.org/10.1016/j.jmrt.2020.06.017.
[47] H. Mehrer, M. Luckabauer, W. Sprengel, Self- and Solute Diffusion, Interdiffusion and Thermal Vacancies in the System Iron-Aluminium, Defect Diffus. Forum. 333 (2013) 1–25. https://doi.org/10.4028/www.scientific.net/DDF.333.1.
[48] S.G. Fries, T. Jantzen, Compilation of `CALPHAD' formation enthalpy data Binary intermetallic compounds in the COST 507 Gibbsian database, Thermochim. Acta. (1998) 12.
[49] C. Flament, Etude des évolutions microstructurales sous irradiation de l'alliage d'aluminium 6061-T6, Université Grenoble Alpes, 2015.
[50] Fang, Song, Li, Du, Precipitation sequence of an aged Al-Mg-Si alloy, J Min Met. Sect B-Met. 46 (2010) 171–180.
[51] E. Clouet, A. Barbu, L. Lae, G. Martin, Precipitation kinetics of AlZr and AlSc in aluminum alloys modeled with cluster dynamics, Acta Mater. 53 (2005) 2313–2325. https://doi.org/10.1016/j.actamat.2005.01.038.
[52] J.R. Croteau, S. Griffiths, M.D. Rossell, C. Leinenbach, C. Kenel, V. Jansen, D.N. Seidman, D.C. Dunand, N.Q. Vo, Microstructure and mechanical properties of Al-Mg-Zr alloys processed by selective laser melting, Acta Mater. 153 (2018) 35–44. https://doi.org/10.1016/j.actamat.2018.04.053.
[53] K.E. Knipling, D.C. Dunand, D.N. Seidman, Nucleation and Precipitation Strengthening in Dilute Al-Ti and Al-Zr Alloys, Metall. Mater. Trans. A. 38 (2007) 2552–2563. https://doi.org/10.1007/s11661-007-9283-6.
[54] K.E. Knipling, D.C. Dunand, D.N. Seidman, Precipitation evolution in Al–Zr and Al–Zr–Ti alloys during isothermal aging at 375–425°C, Acta Mater. 56 (2008) 114–127. https://doi.org/10.1016/j.actamat.2007.09.004.
[55] A.V. Mikhaylovskaya, A.G. Mochugovskiy, V.S. Levchenko, N.Yu. Tabachkova, W. Mufalo, V.K. Portnoy, Precipitation behavior of L12 Al3Zr phase in Al-Mg-Zr alloy, Mater. Charact. 139 (2018) 30–37. https://doi.org/10.1016/j.matchar.2018.02.030.
[56] A. Mehta, J. Dickson, R. Newell, D.D. Keiser, Y. Sohn, Interdiffusion and Reaction Between Al and Zr in the Temperature Range of 425 to 475 °C, J. Phase Equilibria Diffus. 40 (2019) 482–494. https://doi.org/10.1007/s11669-019-00729-9.
[57] Y. Du, Y.A. Chang, B. Huang, W. Gong, Z. Jin, H. Xu, Z. Yuan, Y. Liu, Y. He, F.-Y. Xie, Diffusion coefficients of some solutes in fcc and liquid Al: critical evaluation and correlation, Mater. Sci. Eng. A. 363 (2003) 140–151. https://doi.org/10.1016/S0921-5093(03)00624-5.

[58] K.E. Knipling, D.N. Seidman, D.C. Dunand, Ambient- and high-temperature mechanical properties of isochronally aged Al–0.06Sc, Al–0.06Zr and Al–0.06Sc–0.06Zr (at.%) alloys, Acta Mater. 59 (2011) 943–954. https://doi.org/10.1016/j.actamat.2010.10.017.
[59] Z. Jia, J. Røyset, J.K. Solberg, Q. Liu, Formation of precipitates and recrystallization resistance in Al–Sc–Zr alloys, Trans. Nonferrous Met. Soc. China. 22 (2012) 1866–1871. https://doi.org/10.1016/S1003-6326(11)61399-X.
[60] M.J. Jones, F.J. Humphreys, Interaction of recrystallization and precipitation: The effect of Al3Sc on the recrystallization behaviour of deformed aluminium, Acta Mater. 51 (2003) 2149–2159. https://doi.org/10.1016/S1359-6454(03)00002-8.
[61] A. Deschamps, Y. Brechet, Influence of predeformation and ageing of an Al-Zn-Mg alloy II : Modeling of precipitation kinetics and yield stress, (1999) 13.
[62] M.J. Starink, S.C. Wang, A model for the yield strength of overaged Al–Zn–Mg–Cu alloys, Acta Mater. 51 (2003) 31–50.
[63] S. Thangaraju, M. Heilmaier, B.S. Murty, S.S. Vadlamani, On the Estimation of True Hall-Petch Constants and Their Role on the Superposition Law Exponent in Al Alloys, Adv. Eng. Mater. 14 (2012) 892–897. https://doi.org/10.1002/adem.201200114.
[64] E.O. Hall, The Deformation and Ageing of Mild Steel: III Discussion of Results, Proc. Phys. Soc. Sect. B. 64 (1951) 747–753. https://doi.org/10.1088/0370-1301/64/9/303.
[65] N.J. Petch, The Cleavage Strength of Polycrystals, Iron Steel Inst Lond. 173 (1953).
[66] Y. Bréchet, J. Philibert, A. Vignes, P. Combrade, Métallurgie du minerai au matériau, Dunod, 2013.
[67] M.S.K.K.Y. Nartu, T. Alam, S. Dasari, S.A. Mantri, S. Gorsse, H. Siller, N. Dahotre, R. Banerjee, Enhanced tensile yield strength in laser additively manufactured Al0.3CoCrFeNi high entropy alloy, Materialia. 9 (2020) 100522. https://doi.org/10.1016/j.mtla.2019.100522.
[68] S. Zhang, H. Zhu, L. Zhang, W. Zhang, H. Yang, X. Zeng, Microstructure and properties in QCr0.8 alloy produced by selective laser melting with different heat treatment, J. Alloys Compd. 800 (2019) 286–293. https://doi.org/10.1016/j.jallcom.2019.06.018.
[69] B. Selva Babu, S. Sathiyaraj, A.K.P. Ramesh, B.A. Afridi, K. Kristo Varghese, Investigation of machining characteristics of aluminium 6061 by wire cut EDM process, Mater. Today Proc. (2020) S2214785320383218. https://doi.org/10.1016/j.matpr.2020.10.698.
[70] P. Cao, M. Qian, D.H. StJohn, Effect of iron on grain refinement of high-purity Mg–Al alloys, Scr. Mater. 51 (2004) 125–129. https://doi.org/10.1016/j.scriptamat.2004.03.039.
[71] W. Lefebvre, N. Masquelier, J. Houard, R. Patte, H. Zapolsky, Tracking the path of dislocations across ordered Al3Zr nano-precipitates in three dimensions, Scr. Mater. 70 (2014) 43–46. https://doi.org/10.1016/j.scriptamat.2013.09.014.
[72] Ardell, A.J., Precipitation hardening, Metall. Trans. A. 16A (1985).
[73] S. Gorsse, C. Hutchinson, M. Gouné, R. Banerjee, Additive manufacturing of metals: a brief review of the characteristic microstructures and properties of steels, Ti-6Al-4V and high-entropy alloys, Sci. Technol. Adv. Mater. 18 (2017) 584–610. https://doi.org/10.1080/14686996.2017.1361305.
[74] P.A. Hooper, Melt pool temperature and cooling rates in laser powder bed fusion, Addit. Manuf. 22 (2018) 548–559. https://doi.org/10.1016/j.addma.2018.05.032.
[75] L.-E. Loh, C.-K. Chua, W.-Y. Yeong, J. Song, M. Mapar, S.-L. Sing, Z.-H. Liu, D.-Q. Zhang, Numerical investigation and an effective modelling on the Selective Laser Melting (SLM) process with aluminium alloy 6061, Int. J. Heat Mass Transf. 80 (2015) 288–300. https://doi.org/10.1016/j.ijheatmasstransfer.2014.09.014.